Chemical Science

ROYAL SOCIETY OF CHEMISTRY

EDGE ARTICLE

View Article Online
View Journal | View Issue



Cite this: *Chem. Sci.*, 2024, **15**, 20338

All publication charges for this article have been paid for by the Royal Society of Chemistry

# Phase transition induced hydrogen activation for enhanced furfural reductive amination over a CoCu bimetallic catalyst†

Yilin Wei,‡[a] Zixu Ma,‡[a] Beibei Liu,[a] Jialin Yang,[a] Dan Wu,[a] Yongsheng Zhang,[a] Yuexing Zhang,*[c] Chunbao Charles Xu[d] and Renfeng Nie*[ab]

Received 2nd September 2024
Accepted 7th November 2024

DOI: 10.1039/d4sc05885b

rsc.li/chemical-science

The synthesis of primary amines from renewable biomass and its derivatives through reductive amination has garnered significant attention. How to construct efficient non-noble-metal catalysts that enable low-temperature catalysis still remains challenging. Herein, we report a Cu-doped Co@$CoO_x$ heterostructure catalyst that features structural Co–$CoCuO_x$ bifunctional sites, which enable room temperature reductive amination of various aldehydes with 1.57–45 times higher efficiency than Co@$CoO_x$, outperforming many reported non-noble and even noble metal catalysts. Experiments and DFT calculations indicate that Cu doping leads to a phase transition of Co from hcp to fcc, while electrons are transferred from Cu to Co, forming a dual active site with electron-rich Co closely interacting with $CoCuO_x$. These electron-rich Co sites demonstrate excellent activity in the activation and dissociation of hydrogen, while the $CuO_x$ component facilitates hydrogen spillover at the $CoCuO_x$ interface, thus resulting in a highly efficient cooperative effect for the furfural (FAL) reductive amination. This work provides general guidance for the rational design of high-performance reductive amination catalysts for biomass upgrading.



## 1 Introduction

The escalating energy and environmental crises caused by huge global fossil consumption have drawn significant attention to the search for renewable resources for chemical and fuel production.[1–3] Biomass has emerged as a promising carbon source in the chemical industry due to its abundant reserves, environmental friendliness, and widespread distribution.[4,5] Among them, FAL, dehydrated from hemicellulose, can be further catalytically upgraded into various chemicals *via* hydrogenation, oxidative amination, *etc.*[6–9] In particular, reductive amination is one of the strategies for synthesizing high-value N-containing chemicals, and its product, furfuryl amine (FFA), is a promising intermediate for the polymer, agrochemical, dye, pigment, pesticide, and pharmaceutical industries.[10,11] Nevertheless, the synthesis of primary amines with high selectivity poses a significant challenge due to the occurrence of numerous side reactions in the process.

Currently, significant efforts have been made to develop efficient and selective catalysts for the reductive amination of biomass-derived aldehydes and ketones. Researchers have developed homogeneous or heterogeneous catalysts based on noble metals such as Ru,[12–17] Pd,[18] Pt,[19] and Rh.[20,21] Although these catalysts have demonstrated good catalytic activity for reductive amination, their widespread application is limited by high cost and low abundance. In the case of non-noble metals, catalysts such as Ni,[22–24] Co,[25–30] and Cu[31,32] have been widely studied. However, they usually require harsh reaction conditions (*e.g.*, elevated temperatures or pressures), which can lead to catalyst challenges such as leaching, instability, and deactivation.[33] Therefore, there is an urgent need to develop an efficient non-noble metal catalyst system that facilitates mild reductive amination of carbonyl compounds with high efficacy.

The catalytic activity and selectivity of reductive amination can be tuned by creating efficient bifunctional active sites, with one site strategically positioned near the other.[34–36] These metal bifunctional sites require appropriate spatial intimacy to meet the cooperative active site requirements for the activation and transformation of reactant molecules. Metal bifunctional sites can be constructed in various structures and forms, including synthesizing dual single atoms,[37] dispersing bimetallic alloys on supports,[38] and grafting metal particles onto metal oxides.[16,39]

[a]*National Key Laboratory of Biobased Transportation Fuel Technology, School of Chemical Engineering, Henan Center for Outstanding Overseas Scientists, Zhengzhou University, Zhengzhou 450001, China. E-mail: rnie@zzu.edu.cn*

[b]*State Key Laboratory of Biocatalysis and Enzyme Engineering, School of Life Sciences, Hubei University, 430062, China*

[c]*College of Chemistry and Chemical Engineering, Dezhou University, Dezhou, 253023, P. R. China. E-mail: zhangyuexing@sdu.edu.cn*

[d]*School of Energy and Environment, City University of Hong Kong, Kowloon, Hong Kong SAR*

† Electronic supplementary information (ESI) available: Additional experimental results. See DOI: https://doi.org/10.1039/d4sc05885b

‡ These authors contributed equally.

Once the highly dispersed metal centers form intimate interfaces with the oxides, the synergistic effects between them enable these catalysts to exhibit excellent performance. For example, the Co–$CoO_x$ bifunctional site, composed of highly dispersed Co (center I) and $CoO_x$ (center II), demonstrates a reaction mechanism where the $CoO_x$ center activates $NH_3$ to generate $NH_2{}^{\delta-}$ species, while $H_2$ dissociates on the Co surface and flows toward $CoO_x$.[40] Despite significant advances in catalyst synthesis, achieving catalytically-efficient structures *via* precisely controlling the spatial intimacy of multiple active sites at the sub-nanoscale remains challenging.

Herein, we constructed a CoCu–$CoCuO_x$ heterojunction by modulating the reduction temperature of the crystal phase. Simultaneously, Cu doping induces the transformation of the Co crystal phase from hcp to fcc, resulting in a metal bifunctional site with electron-rich Co and oxygen-vacancy-rich $CoCuO_x$. This heterojunction catalyst facilitated the reductive amination of FAL at room temperature with $N_2H_4\cdot H_2O$ as the nitrogen source, displaying significantly higher activity compared to its mono Cu and Co counterparts. Compared with $NH_3$, the utilization of $N_2H_4\cdot H_2O$ as a nitrogen source completely eliminates the hydrogenation of aldehydes to alcohols, and the intermediate with moderate reactivity notably enhances amine selectivity and effectively prevents the occurrence of the imine-induced trimerization side reaction.[12,41,42] The morphology and structure of the catalyst were thoroughly characterized, and a structure–performance relationship was established. Furthermore, the catalyst's recyclability and substrate tolerance were investigated. Finally, the reaction process and mechanism were explored through *in situ* FTIR, DFT, and kinetic studies. This study presents a novel approach for the efficient and selective synthesis of primary amines from carbonyl compounds under extremely mild conditions without the aid of noble metal catalysts.

## 2 Results and discussion

### 2.1 Catalyst characterization

We synthesized the bimetallic CoCu@$CoCuO_x$ catalyst (Co/Cu feeding ratio of 8/2) *via* a coprecipitation process (Fig. 1a). Typically, salts and base were dissolved separately in deionized water, and the two solutions were mixed to produce $CoCu(CO_3)_x(OH)_y$ precipitation. After calcination, the solid is transformed into oxidized $CoCuO_x$, which can be partially reduced at 250 °C to form the CoCu@$CoCuO_x$ catalyst based on the $H_2$-TPR profile (Fig. S1†), with a specific surface area of 20 $m^2\ g^{-1}$ (Fig. S2†), 62.9% Co and 16.1% Cu loadings determined by ICP-OES (Table S1†), well consistent with the theoretical values.

The crystalline structure of CoCu@$CoCuO_x$ was characterized using XRD (Fig. 1b). Co@$CoO_x$ exhibits four distinct diffraction peaks at 41.6°, 44.7°, 47.5°, and 75.9°, corresponding to (100), (002), (101), and (110) crystal planes of the Co hcp phase (PDF#05-0727). Additionally, a diffraction peak attributed to the (111) crystal plane of CoO (PDF#48-1719) appears at 36.5°, indicating the coexistence of Co and CoO in Co@$CoO_x$. As for CoCu@$CoCuO_x$, the diffraction peaks corresponding to the Co hcp phase disappear, and a new peak appears at 44.2°, corresponding to the (111) crystal plane of the Co fcc phase (PDF#15-0806). However, no diffraction peaks related to metallic Cu are observed, which may be due to more uniformly distributed Cu in the bimetallic catalyst. These results reveal that the Co phase transition from the hcp to fcc phase is promoted by Cu doping with $H_2$ reduction at a temperature of 250 °C.

Surface oxides were characterized by Raman spectroscopy, as shown in Fig. 1c. Co@$CoO_x$ exhibits five typical Raman peaks at 180, 457, 503, 585, and 660 $cm^{-1}$, corresponding to the $F^1_{2g}$, $E_g$, $F^2_{2g}$, $F^3_{2g}$, and $A_{1g}$ modes of CoO.[43] Cu@$CuO_x$ mainly shows three characteristic Raman peaks at 277, 323, and 602 $cm^{-1}$, corresponding to the $A_g$, $B_{1g}$, and $B_{2g}$ vibration modes of CuO. CoCu@$CoCuO_x$ primarily displays two peaks, with the peak at 531 $cm^{-1}$ corresponding to the vibration of $Cu_2O$, and the peak at 676 $cm^{-1}$ corresponding to the $A_{1g}$ vibration mode of CoO.[44] It is worth noting that the $A_{1g}$ mode Raman peak of CoO in CoCu@$CoCuO_x$ shows a pronounced redshift compared to Co@$CoO_x$, which is attributed to lattice distortion induced by abundant oxygen vacancies (Fig. S3, S4 and Table S2†).[45]

The composition and chemical states of the catalysts were characterized using XPS spectra (Fig. 1d, e and S5†). Co 2p XPS spectra (Fig. 1d) confirm the coexistence of $Co^0$ and $Co^{2+}$ for both Co@$CoO_x$ and CoCu@$CoCuO_x$. Compared to Co@$CoO_x$, the Co 2p spectrum of CoCu@$CoCuO_x$ shifts towards lower binding energies, and the ratio of $Co^0/Co^{2+}$ in CoCu@$CoCuO_x$ is 1.49, higher than that in Co@$CoO_x$ (0.47) (Table S2†), indicating electron transfer from Cu to Co and the generation of more $Co^0$ species.[46] As for Cu 2p spectra (Fig. 1e), $Cu^{0/+}$ and $Cu^{2+}$ are detected for both Cu@$CuO_x$ and CoCu@$CoCuO_x$. Compared to Cu@$CuO_x$, the Cu 2p spectrum of CoCu@$CoCuO_x$ shifts towards higher binding energies, indicating electron loss from Cu. The shift of Cu 2p towards higher binding energy corresponds to the shift of Co 2p towards lower binding energy, suggesting that electron transfer occurs from Cu to Co, as confirmed by DFT calculations (Fig. S6†). This electron redistribution contributes to the interaction with the substrate (Fig. S7 and Table S3†) and improves the catalytic activity of the CoCu@$CoCuO_x$ catalyst.[47]

Fig. 1f–k show the low-resolution TEM images of CoCu@$CoCuO_x$, Co@$CoO_x$, and Cu@$CuO_x$, respectively, all of which display porous particles with a size of around 50 nm. To gain a deeper understanding of the surface microstructure, high-resolution TEM imaging was performed. As for Co@$CoO_x$ (Fig. 1j), lattice fringe spacings of 0.203 nm and 0.246 nm can be observed, corresponding to the (002) and (111) crystal planes of hcp Co and CoO, respectively. In the case of Cu (Fig. 1k), Cu species exist mainly in the form of $Cu^0$, with a lattice fringe spacing of 0.208 nm corresponding to the (111) crystal plane of Cu. As shown in Fig. 1g and h, the HR-TEM image and SAED patterns of CoCu@$CoCuO_x$ show lattice fringe spacings of 0.207 nm and 0.246 nm, corresponding to the (111) crystal planes of fcc Co and CoO, respectively, confirming the Co phase transition promoted by Cu doping. Furthermore, the high-angle annular dark-field (HAADF) image and the corresponding EDS elemental mapping of CoCu@$CoCuO_x$ (Fig. 1i) demonstrate the uniform distribution of Co, Cu, and O elements on the catalyst surface.

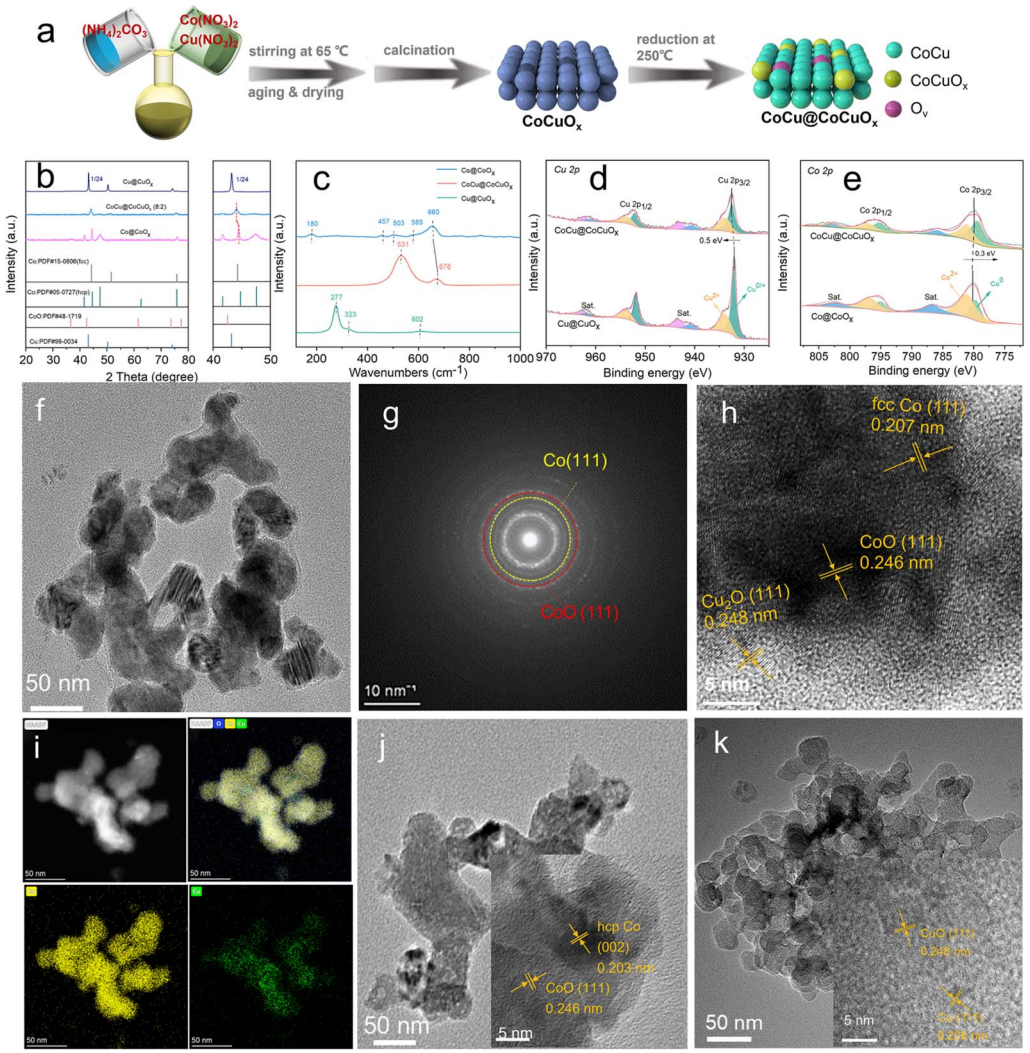


Fig. 1 (a) Schematic illustration for the preparation procedure of $CoCu@CoCuO_x$. (b) XRD patterns, (c) Raman spectra, (d) Co 2p XPS, and (e) Cu 2p XPS spectra of $CoCu@CoCuO_x$, $Co@CoO_x$ and Cu catalysts. TEM and HRTEM images of (f and h) $CoCu@CoCuO_x$, (j) $Co@CoO_x$ and (k) $Cu@CuO_x$ catalysts. (g) SEAD pattern and (i) EDS elemental mapping of $CoCu@CoCuO_x$.

### 2.2 Catalyst performance for FAL reductive amination

Initially, with methanol as the optimal solvent (Fig. S8†), the catalytic performance of $CoCu@CoCuO_x$ with different levels of Cu doping in the FAL reductive amination was compared at 30 °C (Fig. 2a). The FAL conversion reaches 100% for all catalysts at 12 h. When employing the $Co@CoO_x$ catalyst, the FFA yield is only 27.5%. As the Cu doping level increases, the FFA yield initially increases and then decreases. At a $n(Co):n(Cu)$ ratio of 8 : 2, $CoCu@CoCuO_x$ (8 : 2) exhibits the highest FFA yield (94.5%). However, at a $n(Co):n(Cu)$ ratio of 7 : 3, the selectivity of int. 3 and int. 4 increases, while the FFA yield decreases to 68%. In the case of the $Cu@CuO_x$ catalyst, no FFA is observed, probably due to the lack of active sites for imine hydrogenation. In contrast the commercial RANEY® Ni catalyst achieved only a 24.8% yield of FFA under the same reaction conditions. Therefore, $CoCu@CoCuO_x$ (8 : 2) is identified as the optimal catalyst.

The time profiles of FAL reductive amination for $Co@CoO_x$, $CoCu@CoCuO_x$, and $Cu@CuO_x$ were further studied at 30 °C (Fig. 2b–d). As for $Co@CoO_x$ (Fig. 2b), no FFA is observed within 2 h, with yields of int. 3 and int. 4 being 82.9% and 17.1%, respectively. As the reaction time extends to 4 h, FFA gradually forms with a 1.6% yield, while the yields of int. 3 and int. 4 are 58.4% and 40%, respectively. Further prolonging reaction time to 12 h, the FFA yield increases to 27.5%, while the yields of int. 3 and int. 4 decrease to 39.9% and 32.6%, respectively. The $CoCu@CoCuO_x$ catalyst demonstrates significantly improved activity in comparison to $Co@CoO_x$ (Fig. 2c). After 4 h, the FFA yield reaches 29.2%, much higher than that observed with $Co@CoO_x$ (1.6%). When the reaction time reaches 12 h, the FFA yield increases to 94.5%, with the yield of int. 4 at 2.7% and the generation of 2.8% THFOL, mainly due to the over-hydrogenation of the furan ring. Comparatively, no FFA was observed throughout the entire reaction process for $Cu@CuO_x$ (Fig. S9†). Furthermore, the FFA production rates for different

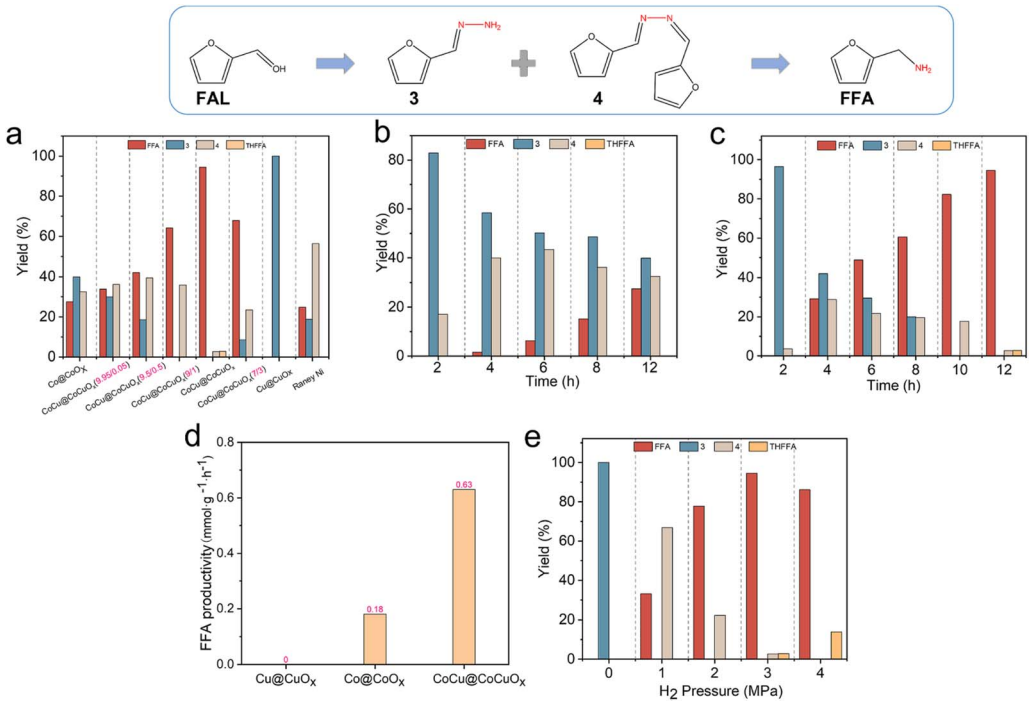


Fig. 2 (a) Effects of Cu doping on the FAL reductive amination. Time curves of FAL amination reaction over (b) Co@$CoO_x$ and (c) CoCu@$CoCuO_x$. (d) FFA productivity rate on three catalysts. (e) Effects of hydrogen pressure on the FAL reductive amination. Reaction conditions: FAL 0.24 mmol, $N_2H_4 \cdot H_2O$ 2 mmol, methanol 4 mL, $H_2$ 3 MPa, 30 °C, catalyst 30 mg, 12 h. Note: FAL was fully converted in this figure.

catalysts were calculated (Fig. 2d), and it was found that the value is 0.63 mmol $g^{-1}$ $h^{-1}$ when using the CoCu@$CoCuO_x$ catalyst, which is 3.5 times higher than that of Co@$CoO_x$ (0.18 mmol $g^{-1}$ $h^{-1}$), further confirming the unique superiority of the bimetallic catalyst CoCu@$CoCuO_x$ for reductive amination.

Next, the influence of hydrogen pressure on the reaction was studied (Fig. 2e). In the absence of $H_2$, only int. 3 is detected. With an increase in hydrogen pressure, the FFA yield gradually increases, reaching a maximum yield of 94.5% at 3 MPa, and then decreases to 86.1% at 4 MPa, accompanied by 13.9% THFOL due to excessive hydrogenation. The type of nitrogen source also significantly affects the reaction (Fig. S10†). When ammonia and hydroxylamine are used as nitrogen sources, the FFA yields are 19.7% and 0%, respectively, which are much lower than that achieved with hydrazine hydrate, mainly due to the less active int. 3 and a simplified reaction network when using hydrazine hydrate. Moreover, both the hydrazine hydrate dosage and catalyst dosage also affect the reaction rate and product distribution (Fig. S11 and S12†). Based on the corresponding optimization, 2 mmol of hydrazine hydrate and 30 mg of catalyst are determined to be the optimal reaction conditions for room-temperature reductive amination. Compared with the reported literature (Fig. 2a and Table S4†), CoCu@$CoCuO_x$ demonstrates comparable FFA yield and productivity for FAL reductive amination under much milder conditions compared to non-noble Co and Ni catalysts (≥60 °C), and it even surpasses the performance of noble Ru and Pt catalysts, particularly at high temperatures exceeding 80 °C.[16,48]

CoCu@$CoCuO_x$ exhibited exceptional activity in selective reductive amination involving FAL, benzaldehyde, 2-octanone, 3-phenylpropanal, and cyclohexanone, with primary amine yields exceeding 95% (Fig. 3a–e). Notably, CoCu@$CoCuO_x$ is much effective than Co@$CoO_x$ and Cu@$CuO_x$. For instance, Cu@$CuO_x$ is nearly inactive for all substrates, while Co@$CoO_x$ exhibits 1.57–45 times lower primary amine yields regardless of whether the substrate is an aldehyde or a ketone. These results further confirm the remarkable versatility of CoCu@$CoCuO_x$ across various carbonyl compounds (Fig. S13†).

The stability and recyclability of the catalyst are paramount for its potential industrial applications. First, a heat filtration experiment (Fig. S14†) confirms that the FAL reductive amination catalyzed by CoCu@$CoCuO_x$ follows a heterogeneous catalytic reaction pathway. Subsequently, the catalyst was further assessed over five consecutive cycles (Fig. 3f), with the FFA yield decreasing from the initial 94.5% to 82.4%, indicating that the catalyst is recyclable over several cycles. Characterization of the spent catalyst reveals an increase in the proportion of $Co^{2+}$ and $Cu^{2+}$ (Fig. S15–S17†), likely due to partial oxidation during the post-treatment; however, this can be partially regenerated through an *in situ* reduction strategy (Fig. S18†).

### 2.3 Study of the reaction mechanism

The *in situ* FTIR spectra of FAL on different catalysts are shown in Fig. S19.† The absorption peaks at 1440, 1473, and 1570 $cm^{-1}$ correspond to the vibration of the $\nu$(C=C) bond, while the peak at 1671 $cm^{-1}$ corresponds to the vibration of the $\nu$(C=O) bond.[49] Both CoCu@$CoCuO_x$, and Co@$CoO_x$ exhibit a strong adsorption capacity for FAL. To further monitor the FAL evolution on the catalysts, the *in situ* FTIR spectra of FAL in the presence of $NH_3/H_2$ were recorded, as shown in Fig. 4a and b.

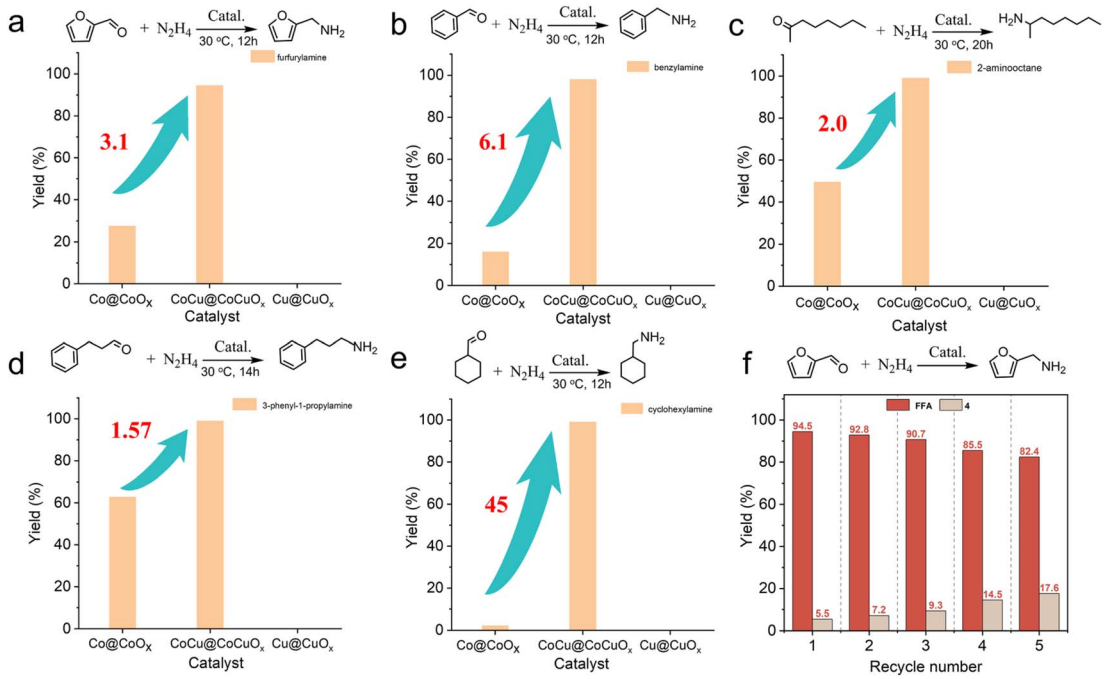


Fig. 3 (a–e) Selective reductive amination of various aldehydes and ketones over Co@CoO$_x$, CoCu@CoCuO$_x$ and Cu@CuO$_x$ catalysts. (f) Catalyst recycling for CoCu@CoCuO$_x$. Reaction conditions: substrate 0.24 mmol, $N_2H_4 \cdot H_2O$ 2 mmol, catalyst 30 mg, methanol 4 mL, 3 MPa $H_2$, 30 °C.

After introducing $NH_3/H_2$, the $\nu$(C=O) bond vibration immediately disappeared, and vibrations corresponding to the$\nu$(C=N) bonds were also observed at 1627 and 1647 cm$^{-1}$, indicating the formation of an imine int. from FAL and $NH_3$. With the passage of reaction time, infrared vibration peaks attributed to $\delta(NH_2)$, $\nu$(C–N), and $\nu$(N–H) appear at 1445, 1557, and 3334 cm$^{-1}$, respectively,[50] indicating that the imine int. is further reduced to FFA. Furthermore, the intensity changes of the $\nu$(N–H) (3334 cm$^{-1}$) vibration related to FFA as a function of time are recorded for Co@CoO$_x$ and CoCu@CoCuO$_x$ (Fig. 4c). It is found the signal intensity of $\nu$(N–H) on CoCu@CoCuO$_x$ increases rapidly with time, indicating that CoCu@CoCuO$_x$ is

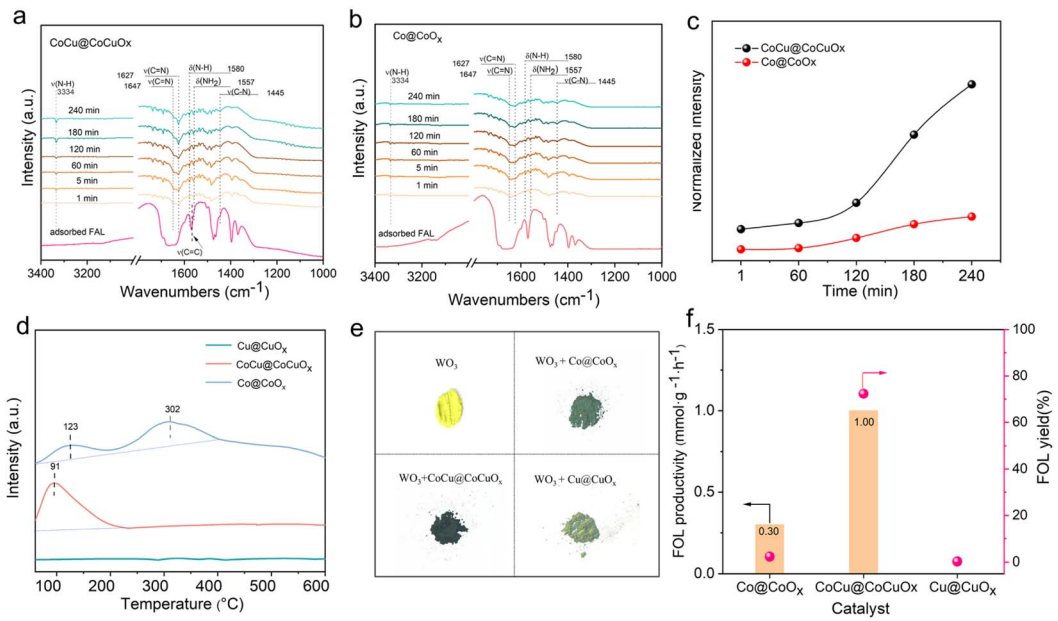


Fig. 4 *In situ* FAL-absorbed FTIR spectra in the presence of $NH_3/H_2$ on (a) CoCu@CoCuO$_x$ and (b) Co@CoO$_x$ catalysts. (c) Intensity evolution of the N–H bond (at 3334 cm$^{-1}$) over CoCu@CoCuO$_x$ and Co@CoO$_x$ catalysts. (d) $H_2$-TPD profiles and (e) hydrogen spillover experiments of Co@CoO$_x$, Cu@CuO$_x$ and CoCu@CoCuO$_x$ catalysts. (f) Reaction rate comparison of FAL hydrogenation over Co@CoO$_x$, Cu@CuO$_x$ and CoCu@CoCuO$_x$ catalysts. Reaction conditions: FAL 0.24 mmol, catalyst 30 mg, methanol 4.0 mL, $H_2$ 3 MPa, 30 °C, 6 h.

more active for FAL reductive amination than Co@$CoO_x$ at ambient temperature and pressure.

To determine whether the substrate adsorption is the most crucial factor or not, the acid properties of the catalysts were studied by $NH_3$-TPD (Fig. S20†) and pyridine-adsorbed IR (Fig. S21†). It was found that Co@$CoO_x$, CoCu@$CoCuO_x$, and Cu@$CuO_x$ exhibit the same Lewis acid sites, with the acid strength following the trend: Co@$CoO_x$ > CoCu@$CoCuO_x$ > Cu@$CuO_x$; this indicates that acid properties cannot explain the differences in their performance difference. It has beeen reported that oxygen defects play a crucial role in substrate adsorption and activation due to their special electronic structure.[51] However, Co@$CoO_x$, CoCu@$CoCuO_x$, and Cu@$CuO_x$ exhibit comparative EPR signal intensities at $g = 2.00$ (Fig. S3†), indicating similar concentrations of oxygen vacancies in all three catalysts, which is also verified using O 1s XPS spectra (Fig. S4†), where vacancy oxygen accounts for 42–62% of all oxygen species. Especially, although Cu@$CuO_x$ contains abundant oxygen defects, no desired amine was detected during the reductive amination, further excluding the vital role for determining the activity differences.

Hydrogen activation, dissociation and migration are also of importance for catalytic reductive amination.[52] $H_2$-TPD profiles (Fig. 4d) show that Co@$CoO_x$ exhibits two $H_2$ desorption peaks located at 123 and 302 °C. In contrast, the desorption peak of CoCu@$CoCuO_x$ shifts to a lower temperature (91 °C) and exhibits significantly enhanced intensity, primarily attributed to the enhanced hydrogen spillover on the catalyst. However, for the Cu@$CuO_x$ catalyst, no significant peaks are observed, indicating the lack of hydrogen activation ability for the monometallic Cu catalyst. The $WO_3$ coloration experiment shows that the color of $WO_3$ changes to green and pale green when Co@$CoO_x$ and Cu@$CuO_x$ are added (Fig. 4e), respectively; while the color change of $WO_3$ is more pronounced, turning almost dark green in the presence of CoCu@$CoCuO_x$, indicating a significant amount of active hydrogen spillover.[53]

To gain a deeper understanding of the impact of Cu doping on hydrogen activation, FAL hydrogenation was used as a probe reaction. As shown in Fig. 4f, Co@$CoO_x$ and Cu@$CuO_x$ exhibit weaker hydrogenation ability toward C=O, with FOL yields of 2.3% and 0.2%, respectively. In comparison, when CoCu@$CoCuO_x$ is used as the catalyst, the FOL yield reaches 72.3%. Through calculations, it is found that the FOL production rate of CoCu@$CoCuO_x$ is 1.00 mmol $g^{-1}$ $h^{-1}$, much higher than those of Co@$CoO_x$ (0.3 mmol $g^{-1}$ $h^{-1}$) and Cu@$CuO_x$ (0 mmol $g^{-1}$ $h^{-1}$). These confirm the synergistic effect between Co and Cu bimetallic species, which effectively promotes the activation of $H_2$ on the catalyst surface, which accelerates hydrogen migration and favors the subsequent hydrogenation.

Periodic density functional theory (DFT) calculations were further performed on CoCu@$CoCuO_x$ to elucidate active sites (Fig. 5a, b, S6 and S7†). Based on the XRD pattern (Fig. 1b) and HRTEM images (Fig. 1f–k), hcp Co (101), fcc Co (111) and Cu (111) crystals were used to simulate the hydrogen activation sites in Co@$CoO_x$, CoCu@$CoCuO_x$ and Cu@$CuO_x$, respectively. It is found that the adsorption energies of $H_2$ on hcp Co (101) and fcc Co (111) are similar, at −0.547 eV and −0.516 eV,

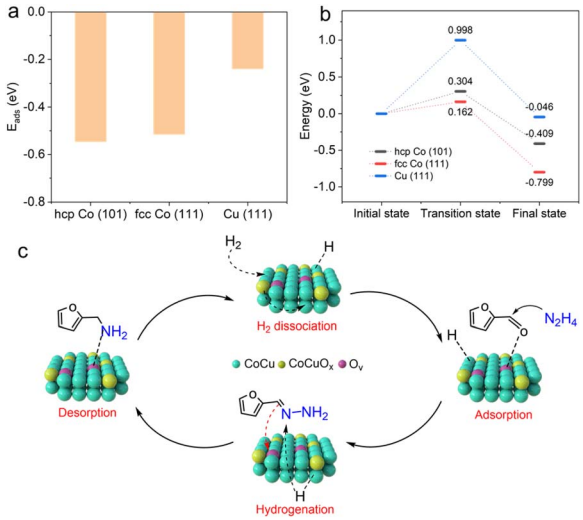


Fig. 5 (a) Calculated adsorption energies of $H_2$ and (b) dissociation energy of $H_2$ on hcp Co (101), fcc Co (111), and Cu (111) surfaces and the (c) reaction mechanism of FAL reductive amination on CoCu@$CoCuO_x$.

respectively (Fig. 5a), but significantly higher than that on Cu (111) (−0.241 eV). Further investigation (Fig. 5b) revealed that the dissociation energy of $H_2$ on fcc Co (111) is 0.162 eV, much lower than that on hcp Co (101) (0.304 eV) and Cu (111) (0.998 eV). Additionally, the reaction energy for the dissociation of active hydrogen on fcc Co (111) is much larger (0.799 eV). These observations, combined with the low activity of Cu@$CuO_x$, suggest that the fcc Co phase present in CoCu@$CoCuO_x$ has stronger hydrogen activation and dissociation capabilities.

Based on the preceding results, a plausible reaction pathway for FAL reductive amination on CoCu@$CoCuO_x$ is proposed (Fig. 5c). Initially, FAL undergoes condensation with hydrazine hydrate to form int. 3. Then the C=N bond of int. 3 is adsorbed and activated by the oxygen vacancies on $CoCuO_x$, while $H_2$ is adsorbed onto the electron-rich fcc Co site, generating active hydrogen species. Moreover, the presence of $CuO_x$ facilitates the migration of active hydrogen from the Co surface to the $CoCuO_x$ surface. Ultimately, the C=N bond in int. 3 is reduced by the active hydrogen on the catalyst, leading to the production of FFA.

## 3 Conclusions

In summary, we demonstrated that the Cu-doped Co@$CoO_x$ heterogeneous interface catalyst contains Co–$CoCuO_x$ bifunctional sites, exhibiting highly active reductive amination capabilities at room temperature, outperforming reported non-noble metal catalysts and even noble metal catalysts. Experimental and DFT calculation results indicate that Cu doping leads to a phase transition of Co from hcp to fcc, while electrons are transferred from Cu to Co, forming a dual active site with electron-rich Co closely interacting with $CoCuO_x$. These electron-rich Co sites show excellent activity in the activation and dissociation of hydrogen, while the $CuO_x$ component

facilitates hydrogen spillover on the $CoCuO_x$ interface. The efficient cooperative effect of CoCu–$CoCuO_x$ enhances the high activity of Co in the room-temperature reductive amination of furfural. This study offers valuable insights into the catalytic mechanism at bifunctional sites and paves the way for developing efficient bifunctional catalysts with a structurally heterogeneous interface for biomass upgrading.

## Data availability

The data supporting this study's findings are available from the corresponding author upon reasonable request.

## Author contributions

R. N. designed the experiments and supervised the project. Y. X. Z. conducted the DFT calculations. Y. W. and Z. M. performed the experiments. All authors discussed the experiments and results. R. N., Y. W. and Z. M. prepared and revised the manuscript.

## Conflicts of interest

There are no conflicts to declare.

## Acknowledgements

The authors acknowledge the financial support from the NSFC (22478366 and U23A20124), the Science and Technology Development Plan Joint Fund Project of Henan Province (232301420048), the Distinguished Young Researchers' Program of Zhengzhou University in China, the Open Funding Project of the State Key Laboratory of Biocatalysis and Enzyme Engineering (SKLBEE20220020) and the Program of Processing and Efficient Utilization of Biomass Resources of Henan Center for Outstanding Overseas Scientists (GZS2022007).

## References

1 D. E. Resasco, B. Wang and D. Sabatini, *Nat. Catal.*, 2018, **1**, 731–735.
2 W.-J. Liu, H. Jiang and H.-Q. Yu, *Energy Environ. Sci.*, 2019, **12**, 1751–1779.
3 G. W. Huber, J. N. Chheda, C. J. Barrett and J. A. Dumesic, *Sci. Adv.*, 2005, **308**, 1446–1450.
4 M. Z. Jacobson and M. A. Delucchi, *Energy Policy*, 2011, **39**, 1154–1169.
5 L. T. Mika, E. Cséfalvay and Á. Németh, *Chem. Rev.*, 2018, **118**, 505–613.
6 S. Chen, R. Wojcieszak, F. Dumeignil, E. Marceau and S. Royer, *Chem. Rev.*, 2018, **118**, 11023–11117.
7 X. Li, P. Jia and T. Wang, *ACS Catal.*, 2016, **6**, 7621–7640.
8 G. Liang, A. Wang, L. Li, G. Xu, N. Yan and T. Zhang, *Angew. Chem., Int. Ed.*, 2017, **56**, 3050–3054.
9 L. Fang, Z. Yan, J. Wu, A. Bugaev, C. Lamberti and M. Pera-Titus, *Appl. Catal., B*, 2021, **286**, 119942.
10 V. Froidevaux, C. Negrell, S. Caillol, J.-P. Pascault and B. Boutevin, *Chem. Rev.*, 2016, **116**, 14181–14224.
11 V. G. Chandrashekhar, W. Baumann, M. Beller and R. V. Jagadeesh, *Chem. Rev.*, 2022, **376**, 1433–1441.
12 H. Zou and J. Chen, *Appl. Catal., B*, 2022, **309**, 121262.
13 V. Boosa, S. Varimalla, M. Dumpalapally, N. Gutta, V. K. Velisoju, N. Nama and V. Akula, *Appl. Catal., B*, 2021, **292**, 120177.
14 D. Deng, Y. Kita, K. Kamata and M. Hara, *ACS Sustainable Chem. Eng.*, 2019, **7**, 4692–4698.
15 D. Chandra, Y. Inoue, M. Sasase, M. Kitano, A. Bhaumik, K. Kamata, H. Hosono and M. Hara, *Chem. Sci.*, 2018, **9**, 5949–5956.
16 C. Xie, J. Song, M. Hua, Y. Hu, X. Huang, H. Wu, G. Yang and B. Han, *ACS Catal.*, 2020, **10**, 7763–7772.
17 T. Komanoya, T. Kinemura, Y. Kita, K. Kamata and M. Hara, *J. Am. Chem. Soc.*, 2017, **139**, 11493–11499.
18 X. Jv, S. Sun, Q. Zhang, M. Du, L. Wang and B. Wang, *ACS Sustainable Chem. Eng.*, 2020, **8**, 1618–1626.
19 Y. Nakamura, K. Kon, A. S. Touchy, K.-i. Shimizu and W. Ueda, *ChemSusChem*, 2015, **7**, 921–924.
20 M. Chatterjee, T. Ishizaka and H. Kawanami, *Green Chem.*, 2016, **18**, 487–496.
21 T. Gross, A. M. Seayad, M. Ahmad and M. Beller, *Org. Lett.*, 2002, **4**, 2055–2058.
22 G. Hahn, P. Kunnas, N. de Jonge and R. Kempe, *Nat. Catal.*, 2019, **2**, 71–77.
23 K. Murugesan, M. Beller and R. V. Jagadeesh, *Angew. Chem., Int. Ed.*, 2019, **58**, 5064–5068.
24 C. Dong, Y. Wu, H. Wang, J. Peng, Y. Li, C. Samart and M. Ding, *ACS Sustainable Chem. Eng.*, 2021, **9**, 7318–7327.
25 R. V. Jagadeesh, K. Murugesan, A. S. Alshammari, H. Neumann, M.-M. Pohl, J. Radnik and M. Beller, *Science*, 2017, **358**, 326–332.
26 M. K. Bhunia, D. Chandra, H. Abe, Y. Niwa and M. Hara, *ACS Appl. Mater. Interfaces*, 2022, **14**, 4144–4154.
27 X. Zhuang, J. Liu, S. Zhong and L. Ma, *Green Chem.*, 2022, **24**, 271–284.
28 M. Elfinger, T. Schönauer, S. L. J. Thomä, R. Stäglich, M. Drechsler, M. Zobel, J. Senker and R. Kempe, *Chem. Sci.*, 2021, **14**, 2360–2366.
29 Z. Yuan, B. Liu, P. Zhou, Z. Zhang and Q. Chi, *J. Catal.*, 2019, **307**, 347–356.
30 B. Zheng, J. Xu, J. Song, H. Wu, X. Mei, K. Zhang, W. Han, W. Wu, M. He and B. Han, *Chem. Sci.*, 2022, **13**, 9047–9055.
31 K. V. R. Chary, K. K. Seela, D. Naresh and P. Ramakanth, *Catal. Commun.*, 2008, **9**, 75–81.
32 H. Yuan, B. T. Kusema, Z. Yan, S. Streiff and F. Shi, *RSC Adv.*, 2019, **9**, 38877–38881.
33 Y. Liu, K. Zhou, H. Shu, H. Liu, J. Lou, D. Guo, Z. Wei and X. Li, *Catal. Sci. Technol.*, 2017, **7**, 4129–4135.
34 Y. Ren, Y. Yang and M. Wei, *ACS Catal.*, 2023, **13**, 8902–8924.
35 C. Cao, W. Guan, Q. Liu, L. Li, Y. Su, F. Liu, A. Wang and T. Zhang, *Green Chem.*, 2024, **26**, 6511–6519.
36 C. Wan, R. Li, J. Wang, D.-g. Cheng, F. Chen, L. Xu, M. Gao, Y. Kang, M. Eguchi and Y. Yamauchi, *Angew. Chem., Int. Ed.*, 2024, **63**, e202404505.

37 R. Li, Z. Zhang, X. Liang, J. Shen, J. Wang, W. Sun, D. Wang, J. Jiang and Y. Li, *J. Am. Chem. Soc.*, 2023, **145**, 16218–16227.
38 E. Hong, S. Bang, J. H. Cho, K.-D. Jung and C.-H. Shin, *Appl. Catal., A*, 2017, **542**, 146–153.
39 L. Ma, K. Sun, M. Luo, L. Yan, Z. Jiang, A.-H. Lu and Y. Ding, *J. Phys. Chem. C*, 2018, **122**, 23011–23025.
40 W. Guo, Z.-Q. Wang, S. Xiang, Y. Jing, X. Liu, Y. Guo, X.-Q. Gong and Y. Wang, *Chin. J. Catal.*, 2023, **47**, 181–190.
41 L. Lv, L. Yu, Z. Qiu and C.-J. Li, *Angew. Chem., Int. Ed.*, 2020, **59**, 6466–6472.
42 Z. Qiu, L. Lv, J. Li, C.-C. Li and C.-J. Li, *Chem. Sci.*, 2019, **10**, 4775–4781.
43 Y. Liu, Y. Zheng, D. Feng, L. Zhang, L. Zhang, X. Song and Z.-A. Qiao, *Angew. Chem., Int. Ed.*, 2023, **62**, e202306261.
44 Y. Zheng, Y. Su, C. Pang, L. Yang, C. Song, N. Ji, D. Ma, X. Lu, R. Han and Q. Liu, *Environ. Sci. Technol.*, 2022, **56**, 1905–1916.
45 Y. Shen, J. Deng, S. Impeng, S. Li, T. Yan, J. Zhang, L. Shi and D. Zhang, *Environ. Sci. Technol.*, 2020, **54**, 10342–10350.
46 Y. Shi, B. Luo, R. Liu, R. Sang, D. Cui, H. Junge, Y. Du, T. Zhu, M. Beller and X. Li, *Angew. Chem., Int. Ed.*, 2023, **62**, e202313099.
47 M. F. Sanad, A. R. Puente Santiago, S. A. Tolba, M. A. Ahsan, O. Fernandez-Delgado, M. Shawky Adly, E. M. Hashem, M. Mahrous Abodouh, M. S. El-Shall, S. T. Sreenivasan, N. K. Allam and L. Echegoyen, *J. Am. Chem. Soc.*, 2021, **143**, 4064–4073.
48 H. Qi, J. K. Yang, F. Liu, L. Zhang, J. Yang, X. Liu, L. Li, Y. Su, Y. Liu, R. Hao, A. Wang and T. Zhang, *Nat. Commun.*, 2021, **12**, 3295.
49 Z. Xue, S. Wu, Y. Fu, L. Luo, M. Li, Z. Li, M. Shao, L. Zheng, M. Xu and H. Duan, *J. Energy Chem.*, 2023, **76**, 239–248.
50 X. Ma, Z. An, H. Song, X. Shu, X. Xiang and J. He, *J. Am. Chem. Soc.*, 2020, **142**, 9017–9027.
51 Y. Wei, Z. Sun, Q. Li, D. Wu, J. Wang, Y. Zhang, C. C. Xu and R. Nie, *Fuel*, 2024, **369**, 131703.
52 B. Li and Z. Xu, *J. Am. Chem. Soc.*, 2009, **131**, 16380–16382.
53 K. Deng, Z. Lian, W. Wang, J. Yu, Q. Mao, H. Yu, Z. Wang, L. Wang and H. Wang, *Appl. Catal., B*, 2024, **352**, 124047.